MATERIALS ENGINEERING

# All-polymeric control of nanoferronics

Beibei Xu,[1] Huashan Li,[2] Asha Hall,[3] Wenxiu Gao,[4] Maogang Gong,[1] Guoliang Yuan,[4] Jeffrey Grossman,[2] Shenqiang Ren[1]*


10.1126/sciadv.1501264

**In the search for light and flexible nanoferronics, significant research effort is geared toward discovering the coexisting magnetic and electric orders in crystalline charge-transfer complexes. We report the first example of multiferroicity in centimeter-sized crystalline polymeric charge-transfer superstructures that grow at the liquid-air interface and are controlled by the regioregularity of the polymeric chain. The charge order–driven ferroic mechanism reveals spontaneous and hysteretic polarization and magnetization at the donor-acceptor interface. The charge transfer and ordering in the ferroic assemblies depend critically on the self-organizing and molecular packing of electron donors and acceptors. The invention described here not only represents a new coupling mechanism of magnetic and electric ordering but also creates a new class of emerging all-organic nanoferronics.**

## INTRODUCTION

Electron transfer and the generation of a new set of $S = {}^1/_2$ spins with exchange interaction in charge-transfer (CT) complexes ($D^0A^0 \leftrightarrow D^{\delta+}A^{\delta-}$) enable a unique coupling between electric and magnetic order parameters, which is important to unlock numerous exciting technological advances in the field of flexible magnetoelectrics (ME) (*1*–*3*). Over the past decades, numerous functional crystalline CT complexes with customized chemical functionality have been developed on the basis of the combination of their unique physical properties and structural stacking factors (*4*–*13*). The physical properties of crystalline CT complexes appear to be associated with the stacking arrangement (mixed- and segregated-stack) and CT degree (mixed-valence and neutral-ionic systems) between the electron donor (D) and acceptor (A) (*14*). For instance, the discovery of one-dimensional metallic conductivity in segregated-stack tetrathiafulvalene-tetracyanoquinodimethane (D-A) complexes has led to the development of organic metals and superconductors in the absence of a metal atom (*15*–*18*), whereas hydrogen-bonded mixed-stack tetrathiafulvalene–pyromellitic diimide (D-A) CT complexes started the field of room temperature ferroelectric switching originating from intermolecular interactions (*19*). However, obtaining simultaneous ferroic orders and room temperature ME coupling properties in CT complexes remains challenging and represents an important topic in material chemistry and condensed matter science (*20*, *21*), especially for the segregated stacks, in part because of their relatively weak intermolecular interactions. In addition, the lack of scalable growth techniques for large-sized high-quality organic CT crystals represents another challenge for the development of organic multiferroics, particularly the thiophene donor and $C_{60}$ acceptor combinations (*22*). Previous studies have mainly focused on small-scale assembled nanostructures and have been concerned with structure disruption during solvent annealing, which is generally necessary to obtain long-range ordered phases (*2*, *22*). Organic multiferroic CT crystals should have a long-range ordered structure, which facilitates the formation of a closely stacked structure and strong interfacial interaction for CT. The growth of large-sized CT crystals is dictated by the control of homogeneous nucleation to avoid the formation of dense nuclei and by the management of growth conditions to facilitate weak intermolecular interactions for the ordered combination of different organic molecules (fig. S1). Here, we show that the very rich CT and ordering of interfaces enable observation of room temperature multiferroic properties in segregated-stack CT complexes. The CT complexes selected for our study are the conjugated polythiophene donor and fullerene ($C_{60}$) acceptor, which are coassembled for the formation of segregated-stack superstructures. Within this cocrystalline structure, several weak intermolecular interactions are present, such as CT electrostatic interactions, van der Waals forces, and π-π stacking, where the interplay between these interactions enables charge order–induced spontaneous dipolar and spin ordering (*19*, *23*–*25*).

## RESULTS

A modified antisolvent crystallization method combined with solvent vapor evaporation has been developed to enable not only the growth of the largest polythiophene-$C_{60}$ CT superstructures to date but also high-quality crystalline perfection. We select 1,2-dichlorobenzene (1,2-DCB) as the good solvent and acetonitrile as the antisolvent for the CT complex; these miscible organic solvents have different solubilities for polythiophene and $C_{60}$. A schematic representation of this modified antisolvent crystallization process is shown in Fig. 1A and fig. S2. Nucleation starts with the addition of the antisolvent because of the local supersaturation at the interface between the good solvent and the antisolvent. Saturated solvent vapor offers an atmosphere for the control of the homogeneous nucleation of crystals. We attribute the growth of the centimeter-sized CT crystals to the following factors: the wetting surface of the substrate, the high concentration of polythiophene and $C_{60}$ in 1,2-DCB, and the control of the formation of starting nuclear materials at the interface between the good solvent and the antisolvent, as well as mass transport and the control of solvent vapor pressure, which all appear crucial for the growth and alignment of high-quality charge-transfer cocrystal (CTCC) superstructures (Fig. 1B and fig. S3A) (*26*, *27*). Large-sized crystals can only form under these controlled conditions (fig. S1). The phase purity of the as-grown CTCCs is confirmed by x-ray diffraction (XRD; Fig. 1C), where the polythiophene donor is crystallized with a monoclinic structure showing a lattice constant $a = 1.717$ nm, $b = 0.77$ nm, and $c = 0.836$ nm (*28*), whereas the $C_{60}$

[1]Department of Mechanical Engineering and Temple Materials Institute, Temple University, Philadelphia, PA 19122, USA. [2]Department of Materials Science and Engineering, Massachusetts Institute of Technology, Cambridge, MA 02139, USA. [3]U.S. Army Research Laboratory, Aberdeen Proving Ground, Aberdeen, MD 21005, USA. [4]School of Materials Science and Engineering, Nanjing University of Science and Technology, Nanjing 210094, China.
*Corresponding author. E-mail: shenqiang.ren@temple.edu

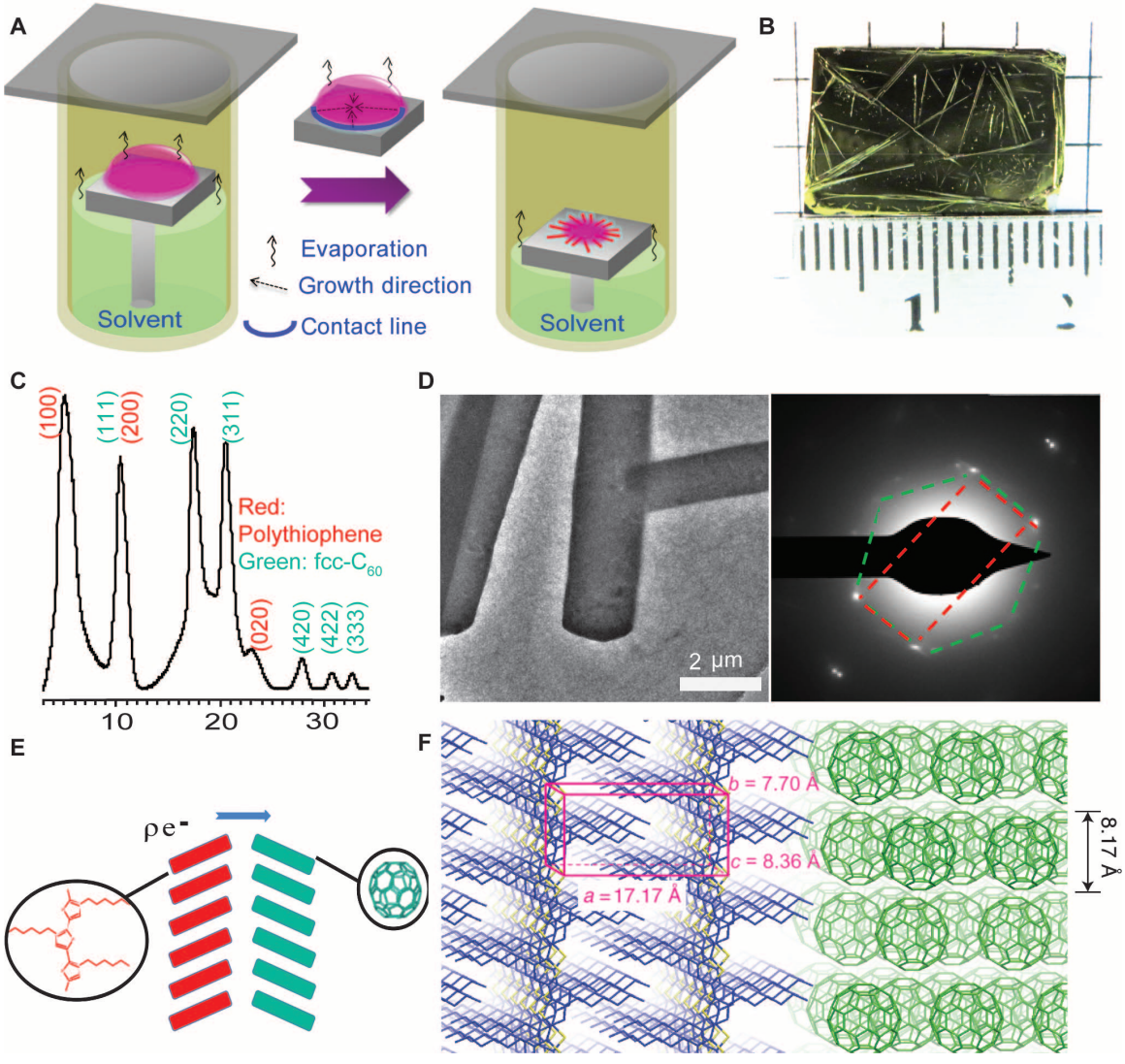


**Fig. 1. Schematic representations of the crystal growth method and structure of the CTCCs.** (**A**) Modified antisolvent crystallization growth scheme combined with solvent vapor evaporation. 1,2-DCB was used as the good solvent and acetonitrile as the antisolvent. Acetonitrile was added to induce localized supersaturation and precipitation of cocrystals at the interface of good solvent and antisolvent. (**B**) Photograph of the as-grown CTCCs. (**C**) XRD spectrum of CTCCs. (**D**) TEM image and SAED pattern of the CTCC. (**E**) Segregated stacking pattern of the CTCCs. (**F**) Schematic structural schemes of the CTCC. Blue denotes the polythiophene backbones and side chains, yellow denotes the S atoms on the backbone of polythiophene, and cyan-green denotes the $C_{60}$ clusters.

acceptor has a face-centered cubic (fcc) structure with a lattice constant of 1.415 nm (*29*). The selected-area electron diffraction (SAED) pattern from transmission electron microscopy (TEM) confirms the coexistence of monoclinic polythiophene and fcc-$C_{60}$ structures (Fig. 1D) with two sets of diffractions, consisting of (001)-monoclinic polythiophene crystal and (111)-fcc-$C_{60}$ crystal, respectively. Within the segregated-stack CTCC superstructures, complicated intermolecular interactions, including π-π stacking, CT, and van der Waals forces, contribute to the stacking and ordering of the polythiophene donor and $C_{60}$ acceptor along the π-π stacking axis of polythiophene (Fig. 1, E and F) (*27*, *30*). Polythiophene chains self-organize through π-π conjugated interactions along the *b* axis (*25*, *27*) and are stacked in planar structures, with the long-chain axis (*c* axis) nearly perpendicular to the substrate (Fig. 1F).

Focusing on the segregated stacking of CTCC superstructures, we have investigated the structural and chemical aspects of the as-grown cocrystals. Figure 2A shows a typical side-view scanning electron microscopy (SEM) image of the CTCCs, where the inset is the carbon and sulfur chemical analysis and mapping by energy-dispersive x-ray spectroscopy. The sulfur content is higher in the center of the CTCCs than in the edge, confirming the phase segregation between the polythiophene donor and the $C_{60}$ acceptor (also shown in the dark-field optical microscopy image; fig. S3, B and C). The TEM and high-resolution TEM images of the CTCCs (shown in Fig. 2B and fig. S4, A to D) confirm the phase intermixing and the segregated stacking of cocrystals with an average domain size of ~20 nm. The polythiophene fibers are crystallized with $C_{60}$-rich domains. The three-dimensional atomic force microscopy (AFM) image (fig. S4, E and F, taken near the

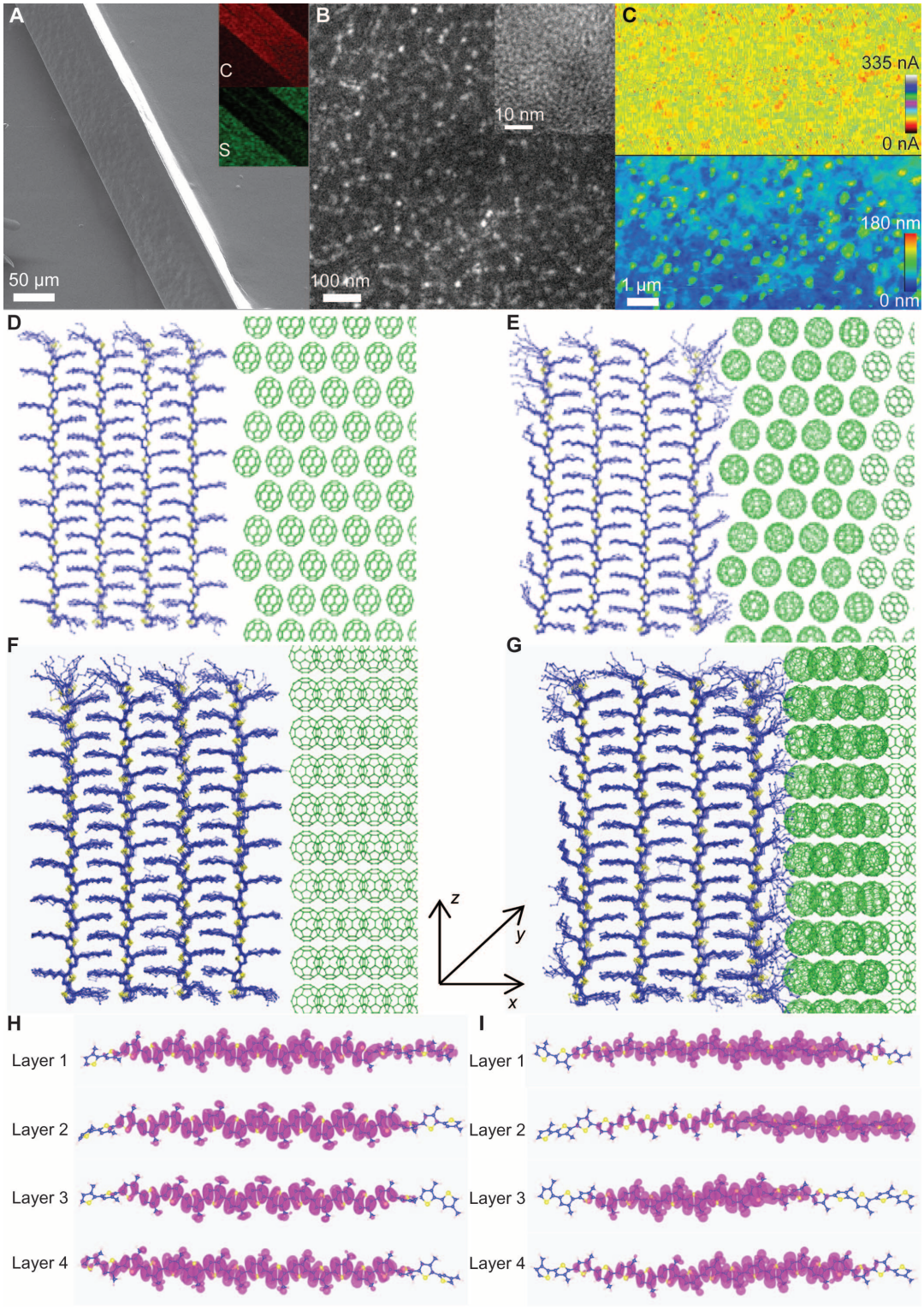


**Fig. 2. Morphology, phase separation, and polythiophene/$C_{60}$ interface configuration of the CTCCs.** (**A**) Typical side-view SEM image of the CTCCs. The inset is the carbon and sulfur chemical analysis mapping from energy-dispersive x-ray spectroscopy. (**B**) TEM image of the center region in the CTCCs. The inset is the high-resolution TEM image. (**C**) Current (top) and topography (bottom) images from the conducting AFM (c-AFM) of the CTCCs. (**D** to **G**) Polythiophene/$C_{60}$ interface configurations obtained by classical MD simulation for configuration 1 with rough surface at $t = 0$ and 1 ns, respectively (D and E), and configuration 2 with flat surface at $t = 0$ and 1 ns, respectively (F and G). (**H** and **I**) Highest occupied molecular orbital of polythiophene molecules at each layer of configuration 1 (H) and configuration 2 (I).

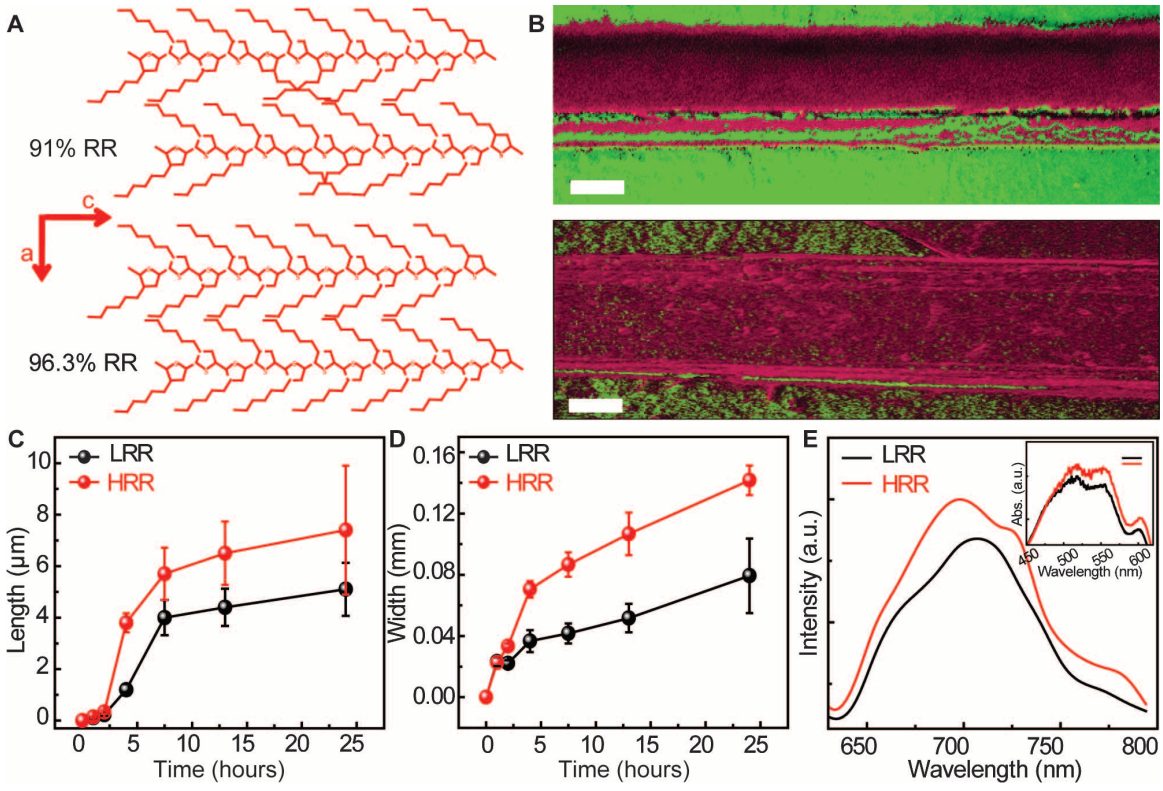


**Fig. 3. The RR of polythiophene-dependent CTCC growth and corresponding optical properties.** (**A**) Molecular structures of 91% (LRR) and 96.3% (HRR) polythiophene. (**B**) Confocal fluorescence microscopy images of CTCC synthesized with LRR (above) and HRR (below) polythiophene. Scale bars, 50 μm. (**C** and **D**) Dimensions in the length and width directions of the time-dependent LRR and HRR CTCC growth. Error bars are attributed to ~20 crystals present on the surface of the substrates. (**E**) Confocal fluorescence spectra of LRR and HRR CTCCs. The excitation wavelength is 488 nm. The inset is the absorption spectra of LRR and HRR CTCCs. a.u., arbitrary units.

center of the CTCCs) reveals a surface separation of the CTCCs due to phase segregation between the polythiophene donor and $C_{60}$ acceptor. The current and topography images obtained by c-AFM confirm the segregation contrast between the donor and the $C_{60}$-rich acceptor phases. To explore the interfacial effects on the charge transport of segregated-stack CTCC superstructures, we used classical molecular dynamics (MD) and density functional theory to investigate the interfacial ordering between the polythiophene and $C_{60}$ phases and its effects on the electrical properties of the polymer (the simulation methods are described in detail in the Supplementary Materials). Furthermore, the extensive modeling uniquely provides an understanding of efficient transport properties even with a large area of interfaces and strong interactions between the donor and the acceptor within a large (centimeter-sized) CTCC crystal. Because the {111} diffraction direction of fcc-$C_{60}$ crystal is aligned with the polymer chain, we considered two interfacial configurations. Each configuration contains four layers of polythiophene and six layers of $C_{60}$ in the *x* direction, wherein the polythiophene molecules were represented by polymer chains containing 18 thiophene rings. The size of the supercell in the *y* direction is determined by the matching of periodicity between the polythiophene and the $C_{60}$ crystal phases. The first configuration consists of 24 polythiophene molecules and 216 $C_{60}$ molecules (Fig. 2, D and E), whereas the second configuration consists of 56 polythiophene molecules and 288 $C_{60}$ molecules (Fig. 2, F and G). The crystal structures of both the polythiophene and $C_{60}$ phases are nearly unaffected by the interface because of the strong interaction between the molecules in each phase. Polythiophene and $C_{60}$ attract each other, but the steric effect between the side chain of polythiophene and $C_{60}$ prevents direct contact between the polythiophene ring and $C_{60}$. Such a scenario is not affected by the size of the system or the interfacial orientation with different surface roughness. Moreover, the final interface configuration is not sensitive to the initial condition of the polythiophene surface (fig. S5). Because of structural robustness, neither energy-level fluctuation nor wavefunction distribution correlate to the distance between the polythiophene molecule and the polythiophene/$C_{60}$ interface, indicating that the energy-level fluctuation originates from the polythiophene crystal itself (the intrinsic fluctuation or artificial boundary effect) rather from the polythiophene/$C_{60}$ interface (Fig. 2, H and I, fig. S6, and table S1). In general, the transport properties of the CT complexes (fig. S1A) are dominated by the hopping mechanism (*22*); by contrast, the transport properties of the large-sized CTCCs are dominated by defects in the crystal. Such desirable electrical properties would not be achieved without the three-dimensional large-sized crystal structure of CT complexes (*22*, *31*).

The study of crucial physical properties requires the growth of high-quality large-sized CTCC superstructures, and this variability is largely influenced by the molecular packing of polythiophene donor phase dictated by its regioregularity (RR). The electrical and optical properties of the pristine polythiophene phase are improved by the degree of RR, which is defined as the percentage of head-to-tail monomers

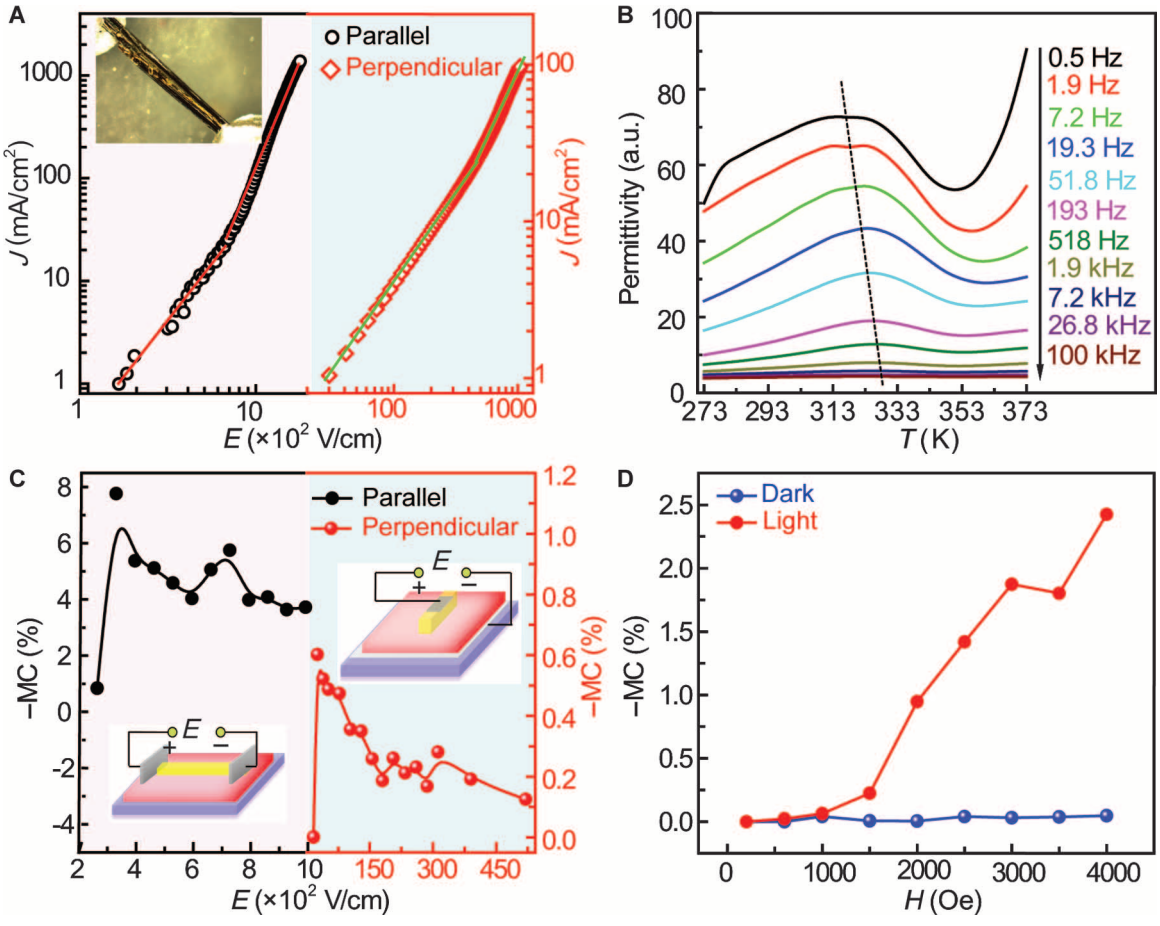


**Fig. 4. Anisotropic electrical and MC properties of the HRR CTCCs.** (**A**) Current density–electric field curves, oriented parallel and perpendicular to the long axis (*b* axis) of the CTCC, respectively. The inset shows the photograph of CTCC between two silver electrodes for the parallel measurements. (**B**) Temperature-dependent permittivity for the selected frequencies of CTCCs. (**C**) Dark MC under different electric fields. The left and right insets are the parallel and perpendicular direction measurement schemes, respectively. (**D**) Dark/light-controlled MC under different magnetic fields in the perpendicular direction. The applied electric field is 13 kV/cm. The light intensity is 70 mW/cm$^2$.

rather than head-to-head configuration (Fig. 3A) (*32*, *33*). Polythiophene with an RR of 91% [low RR (LRR)] and 96.3% [high RR (HRR)] is applied here to demonstrate the influence of the self-organization of polythiophene molecules on the packing of the CTCC superstructures. A higher RR of polythiophene enables closer packing and ordering into planar lamellae structures with an increased interchain character, which leads to a larger high-quality and crystalline CTCC superstructure (*33*). The confocal fluorescence microscopy images stress again the importance of interplane packing density in the growth of CTCC superstructures (Fig. 3B). To further illustrate the relationship between the RR of polythiophene and the nanostructure of CTCCs, we examined the time-dependent crystal growth of the HRR and LRR cocrystals and found that the dimension in both the length and width direction and the density of the HRR cocrystals are larger than those of the LRR cocrystals (Fig. 3, C and D, and figs. S7 and S8). The increased interchain interactions of HRR-induced CTCCs lead to a higher absorption, whereas the increased emission intensity suggests that less nonradiative quenching pathways exist in the more ordered CTCCs (Fig. 3E). It should be noted that the absorption spectra obtained by laser spectroscopy clearly present different absorption bands from those of pristine thin films of polythiophene/$C_{60}$ (fig. S9) (*34*), confirming the existence of ground-state CT in CTCC superstructures. Moreover, the importance of RR in chain packing and ordering also influences the device performance of CTCC superstructures (figs. S10 and S11).

Large-scale free-standing superstructures provide advantageous access to measure anisotropic behaviors because of the long-range ordered structures along different packing orientations, which do not exist in conventionally processed CT complexes (*2*, *22*). These CTCCs have their long axis aligned with the crystallographic *b* axis as demonstrated by the measurement of their highly anisotropic electrical properties. For the in-plane and out-of-plane measurements, the electric field is oriented parallel (*b* axis) and perpendicular (*c* axis) to the cocrystal long axis, respectively. The inset of Fig. 4A shows the photograph of a CTCC cocrystal between two electrodes. To avoid dielectric breakdown of the CTCC superstructures, the electric field in the parallel direction is always smaller than that in the perpendicular direction in the following measurements. The ohmic region of the current-voltage curve (Fig. 4A) is used to examine the resistivity (ρ) along the parallel and perpendicular directions, determined as $6.7 \times 10^6$ and $2.66 \times 10^8$ Ω·m, respectively. The calculated conductivity is close to the experimental

value (fig. S12A). The measured parallel direction is along the π-π stacking direction of the polythiophene chain, exhibiting a larger charge carrier density and mobility. Temperature-dependent electric permittivity, conductivity, and loss tangent at various frequencies (Fig. 4B and fig. S12, A and D) display pronounced transition peak above room temperature, indicating the potential ferroelectric phase transition in the CTCCs (*20*). There are two peaks around 312 and 322 K for the temperature-dependent electric permittivity at low frequency, indicating the phase separation of polythiophene and $C_{60}$ in the segregated-stack CTCCs. These two peaks can also be found in the temperature-dependent conductivity and loss tangent (fig. S12, A and D). The suppressed amplitude with increased frequency (Fig. 4A and fig. S12C) is attributed to the dielectric relaxation, whereas there is a small shift of the transition temperature to 328 K at high frequency, implying the possible existence of dielectric clusters in the CTCC. We evaluate the magnetoconductance (MC) in both the parallel and perpendicular directions to gain further understanding of the anisotropic effect due to their stacking arrangement [MC = [$J$(B) – $J$(0)]/$J$(B), where $J$(B) and $J$(0) are the current density with and without loading magnetic field, respectively]. The Coulomb capture radius defines the distance when the Coulomb attraction energy between the captured electrons and holes is equal to the thermal energy. The radius

$$r = \frac{e^2}{4\pi\varepsilon_0\varepsilon_r\kappa_B T} \quad (1)$$

where $e$ is the charge, $\varepsilon_0$ is the permittivity of vacuum, $\varepsilon_r$ is the relative permittivity of the CTCC cocrystals, $k_B$ is the Boltzmann's constant, and $T$ is temperature (*35*, *36*). The small relative permittivity for our cocrystal results in the large Coulomb capture radius. Figure 4C demonstrates that the MC in the parallel direction is larger than that in the perpendicular direction, which is attributed to magnetic field–reduced spin mixing, leading to the increase of triplet CT through intersystem crossing (*37*, *38*). The scattering reaction between triplet CT states and charge carriers decreases the mobility of charge carriers, resulting in a decrease in the current density under a magnetic field for the negative MC (fig. S13). A large density of charge carriers will be beneficial for the formation of CT states, which contribute to a larger MC effect (*39*, *40*). Therefore, we carried out photoexcitation-dependent MC measurement of CTCCs under the dark and illuminated states (white light of 70 mW/cm$^2$), as shown in Fig. 4D and figs. S14 and S15. Under photoexcitation, a pronounced light intensity–dependent

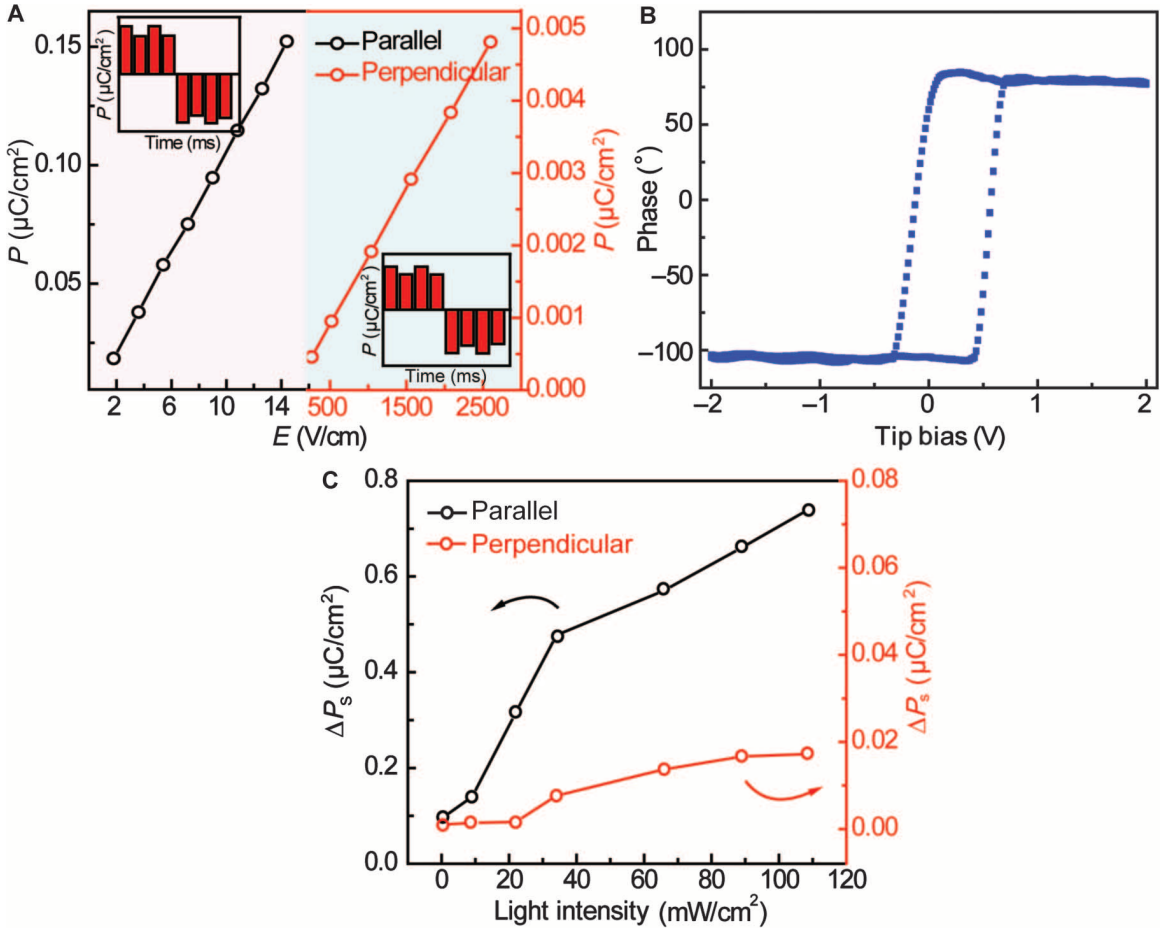


**Fig. 5. Ferroelectric properties of the HRR CTCCs.** (**A**) Electric field–dependent saturation polarization value in the parallel and perpendicular directions. The insets are the PUND polarization measurement of the CTCCs in the parallel (left) and perpendicular (right) directions, respectively. The electric fields of PUND measurement in the parallel and perpendicular directions are 9 and 520 V/cm, respectively. (**B**) Hysteresis loops of the piezoelectric response versus tip bias. (**C**) Light intensity–induced saturation polarization change in the parallel and perpendicular directions.

MC effect is observed as more CT states are tuned by an external magnetic field (fig. S16).

The CT and ordering of hierarchical CTCC superstructures could enable different ferroic order parameters at different scales in which the multifunctionalities emerge. In the CTCC superstructures, electron transfer in a crystalline segregated stack can create a dipole moment where the switching of polarization under an applied electric field occurs (Fig. 5A). The insets of Fig. 5A provide the positive-up negative-down (PUND) measurements along the parallel and perpendicular directions of the cocrystals, which exhibit remanent polarization after removing the electric field, confirming the ferroelectric properties of CTCC superstructures. The charge ordering along the

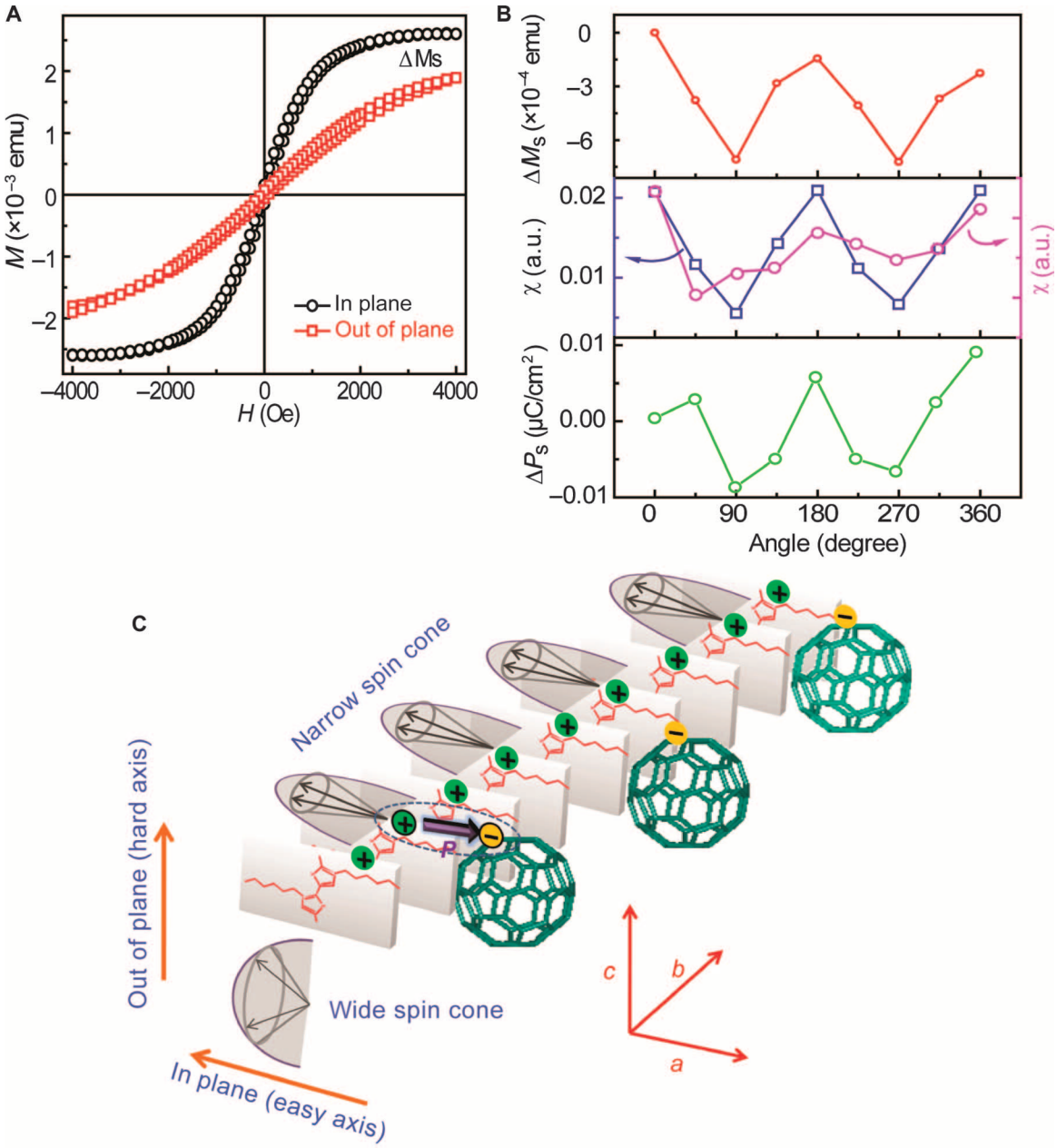


**Fig. 6. Magnetic properties of the HRR CTCCs.** (**A**) M-H loops of the CTCCs in the in-plane and out-of-plane directions. $\Delta M_s$ shows the difference in the saturation magnetization in the two directions. (**B**) Angle-dependent saturation magnetization (top), experimental (middle left) and calculated spin susceptibility (middle right), and saturation polarization (bottom). The electric field is loaded parallel to the CTCC long axis. The external magnetic field for the polarization measurement is 200 Oe. (**C**) Spin cone distribution along the long axis (*b* axis) of the CTCC and the polarization induced by charge ordering and CT at the interface. The direction and width of the spin cone depend on the spin direction and the charge-lattice coupling extent. The positive and negative charges in polythiophene and $C_{60}$ are used for the illustration of CT and dipoles, which do not represent the real charge distribution in the cocrystals.

stacking axis (*b* axis, or in-plane direction) allows a larger polarization than that of the packing along the perpendicular orientation. We have analyzed the ferroelectricity properties of CTCC superstructures using piezoresponse force microscopy (PFM). Figure 5B presents the local hysteresis loops of the piezoelectric response versus tip bias. To ramp the loops, we applied a dc bias voltage through a conductive tip to the CTCC surface from −2 to 2 V at a frequency of 0.3 Hz. The local hysteresis loops for ferroelectric polarization switching confirm the ferroelectric properties of the CTCC superstructures (Fig. 5B and fig. S17). Because the lifetime of singlet excitons is much shorter than that of triplet excitons (microseconds or longer) (*31*), photoexcitation-induced CT states in the CTCC superstructures lead to an increase in triplet excitons (dipoles) or polarization (Fig. 5C).

Anisotropic magnetization of CTCC superstructures was characterized through the angle-dependent magnetic hysteresis (M-H) loops (Fig. 6, A and B, and fig. S19), where the saturation magnetization ($M_s$) displays angle-dependent behavior between the in-plane (easy-axis) and out-of-plane (hard-axis) directions ($\Delta M_s$). Elemental analysis confirms that the magnetic impurities present are well below the detection limits of atomic absorption spectroscopy, which rules out the possibility of impurity-induced magnetization. Large-scale free-standing crystals enable mass collection for the powder-based magnetization measurement, which is not feasible in small-scale assembly (*2*, *22*), as shown in fig. S20. The charge-lattice and electron-phonon coupling in the crystalline polythiophene chain renders the CTCC superstructures magnetic. A narrow spin cone that resulted from the strong charge-lattice coupling promotes the spin alignment along the easy axis because of the charge ordering along the stacking axis (Fig. 6C) (*41*). This spin orientation–dependent behavior leads to magnetization anisotropy between the easy-axis (in-plane) and hard-axis (out-of-plane) directions. To further confirm this orientation-dependent anisotropic behavior, we further investigate the magnetic and spin susceptibility angular dependence (Fig. 6B). By tuning the angle of the magnetic field (when magnetic field is parallel to the easy axis, the angle θ is set at 0°, 180°, or 360° as shown in Fig. 6B), the calculated and experimental susceptibility both exhibit an angle-dependent behavior between the easy-axis and hard-axis directions, confirming the angular-dependent spin cone orientation effect. Moreover, the ordered π-π stacking is beneficial for the charge-lattice coupling with the generation of charge ordering, resulting in the emergence of simultaneous polarization and magnetism, leading to potential ME coupling. Indeed, the angle-dependent polarization follows the magnetic orientation trend, indicating that the charge ordering at the interfaces allows the coupling between magnetic and electric orders in CTCC superstructures.

To confirm the ferroic coupling effect, we examined the ME coupling in CTCC superstructures through electric field–controlled magnetization under a bias magnetic field of 60 Oe (Fig. 7A). The ME coupling coefficient (α) along the parallel direction shows an optimum value of $7.2 \times 10^{-3}$ Oe·cm/V, compared to $0.16 \times 10^{-3}$ Oe·cm/V in the perpendicular direction. The CT and ordering at interfaces lead to polarization and magnetism of CTCC superstructures (*3*, *42*), as well as their ME coupling effect. Therefore, photoexcitation-induced CT and ordering further enhance the ME coupling in CTCC superstructures, with an optimum ME coefficient of $2.33 \times 10^{-2}$ Oe·cm/V (Fig. 7B and figs. S21 and S22). Because CT and ordering occur along the stacking axis, the ME coupling effect along the parallel direction has a higher magnitude than that in the perpendicular orientation. Room temperature ferroic orders and ME coupling of CTCC superstructures provide a platform for the development of all-organic multiferroics.

## DISCUSSION

In conclusion, we have developed for the first time an antisolvent crystallization approach combined with solvent vapor evaporation to organize electron donor polythiophene and $C_{60}$ acceptor intocentimeter-sized segregated-stack CT superstructures for their anisotropic measurement using free-standing crystals. The CT and ordering at interfaces enable the occurrence of simultaneous room temperature anisotropic ferroic orders and their coupling along the stacking axis of the crystalline CT superstructures. The giant anisotropic behavior largely resulted from packing structure along different crystal growth directions, which leads to unique optical properties and extraordinary anisotropic electrical and ME coupling behaviors. Specifically, along the ordered π-π stacking direction of the crystal long axis, the performances are higher than those in other directions. Theoretical simulation uncovers a structural and interfacial mechanism on the crystal structure, energy-level fluctuation, and wavefunction distribution of CT superstructures. Large-scale free-standing CT crystals will constitute a new direction

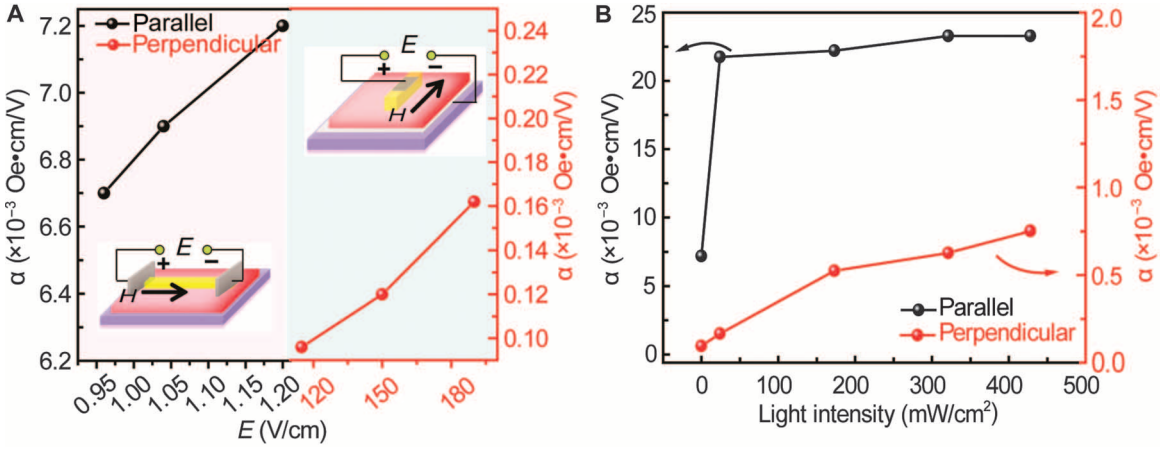


**Fig. 7. ME coupling of HRR CTCCs.** (**A**) ME coupling effect (electric field–dependent magnetization) with a bias magnetic field of 60 Oe. (**B**) Light intensity–dependent ME coupling of CTCCs.

for solution-processable all-organic ferroic devices. In this respect, this work defines a research avenue for alternative materials to those studied extensively in recent years, such as inorganic multiferroic oxides and organic spintronics, and opens a search for suitable carbon-based CT materials with yet untapped potential for efficient ferroic devices. The principle of using crystalline CT compounds offers broad design flexibility, which leads to great potential for the development of room-temperature organic ME multiferroics.

## MATERIALS AND METHODS

### Synthesis of polythiophene-$C_{60}$ solution by an antisolvent crystallization method

Polythiophene (20 mg/ml) [RR of 96.3% (HRR) and 91% (LRR)] was resolved in 1,2-DCB solvent at 60°C for 2 hours. $C_{60}$ was added into the solution at a weight ratio of 1:1 (polythiophene/$C_{60}$) and stirred at room temperature for 10 hours. Then, 10 volume % of acetonitrile antisolvent was added into the solution to facilitate the precipitation of seeds under ambient conditions and sonicated for 5 min at room temperature. The solution was aged for 2 days and stored in a glove box before use. HRR polythiophene was purchased from Ossila Ltd. (M104, RR = 96.3%, $M_w$ = 77,500, $M_n$ = 38,700). LRR polythiophene was purchased from BASF in cooperation with Rieke Metals (Sepiolid P200, RR = 91%, $M_w$ average = 50 to 70 K). $C_{60}$ (purity, 99.5%) was purchased from Sigma-Aldrich.

### Growth of charge-transfer polythiophene-$C_{60}$ cocrystals (CTCCs) by solvent vapor evaporation

$SiO_2$/Si substrate was successively sonicated in soap solution, distilled water, acetone, and isopropanol and dried by $N_2$. The surface was then treated with ultraviolet/ozone for 30 min. After cleaning, poly(3,4-ethylenedioxythiophene):polystyrene sulfonate (PEDOT:PSS) was coated on its surface by spin coating at 3600 rpm for 1 min and dried at 150°C for 30 min. The PEDOT:PSS film was used to increase the adhesion and decrease the surface roughness of the crystals. A high concentration of polythiophene-$C_{60}$ solution was drop-casted onto the substrate under $N_2$ atmosphere. The substrate with the droplet was placed on a Teflon sample holder filled with 1,2-DCB solvent and sealed by parafilm. Under the saturated 1,2-DCB vapor pressure, crystals formed with the slow evaporation of the solvent within 24 hours. Computational methods can be found in part 4 of the Supplementary Materials.

### Conducting AFM

Nanosurf EasyScan 2 FlexAFM was used to obtain the current and topography images on the surface of the cocrystals. The *n*-type Si probe coated with Pt on both sides had a resistivity of 0.01 to 0.025 ohm/cm. The radius of the probe was below 30 nm. The applied voltage was 5 to 10 V.

### Optical microscopy

Confocal fluorescence spectral analysis was carried out with a Zeiss Meta 510 upright confocal microscope with a 488-nm Ar ion laser as the excitation source. The cocrystal samples were grown on a silica substrate.

### Polarization measurement

Radiant Precision Premier LC II was used to measure the polarization hysteresis loops and the PUND at room temperature in air.

### Piezoresponse force microscopy

PFM was measured with an AFM (Bruker MultiMode 8). The images were scanned by a Co/Cr-coated conductive tip (Bruker MESP-RC). The films were spin-coated on a glass substrate.

### Electron spin resonance measurements

Electron spin resonance (ESR) signal and spin susceptibility was obtained by a Bruker EMX (type ER073) plus ESR spectrometer. The cocrystal samples for the ESR measurements were grown on a silica substrate.

### M-H loop measurement

The M-H loops of all cocrystals and powder samples were measured with a MicroSense EV7 vibrating sample magnetometer at room temperature.

### Dielectric constant measurement

A broadband dielectric/impedance spectrometer was used to measure the capacitance in 0 to 100 kHz at 0° to 100°C. The bias was 100 mV.

## SUPPLEMENTARY MATERIALS

Supplementary material for this article is available at http://advances.sciencemag.org/cgi/content/full/1/11/e1501264/DC1

Mass transport–induced crystallization of CTCCs

Fig. S1. Photograph of the crystals.

Fig. S2. Optical microscopy image of the initial growth stage of the crystals.

Fig. S3. Dark-field optical microscopy image of the CTCC.

Fig. S4. High resolution TEM images of CTCCs, and AFM image near the center of the cocrystals.

Classical molecule dynamics (MD) simulations on the interface configuration of polythiophene/$C_{60}$ CTCCs

Fig. S5. Polythiophene/$C_{60}$ interface configuration while polythiophene structure starts from free surface in the *x* direction.

Fig. S6. Polythiophene/$C_{60}$ interface configuration with monolayer or single-molecule polythiophene.

Table S1. Energy-level distribution of polythiophene layer close to the polythiophene/$C_{60}$ interface with multilayer polythiophene crystal and single molecule, respectively.

Time- and RR-dependent crystallization

Fig. S7. Time-dependent crystal growing for 91% RR CTCC.

Fig. S8. Time-dependent crystal growing for 95.7% RR CTCC.

Absorption spectra

Fig. S9. Absorption spectra of CTCCs measured by a microscope in the range of 600 to 1200 nm.

RR-dependent electrical and magnetic properties

Fig. S10. Magnetoconductance.

Fig. S11. ME coupling effect with different loading electric field.

Electrical properties

Fig. S12. Electrical properties as a function of temperature and frequency.

Anisotropic MC effect

Fig. S13. MC of CTCC under different electric fields.

Fig. S14. MC of CTCC under different magnetic fields.

Fig. S15. Light-illuminated MC of CTCC under different magnetic fields.

Fig. S16. Light intensity–dependent MC of vertical.

Piezoelectric response

Fig. S17. Amplitude of the piezoelectric response versus tip bias.

Electron spin resonance

Fig. S18. ESR of CTCC at 80 K and room temperature.

Angle-dependent magnetism

Fig. S19. Angle-dependent M-H loops of CTCC.

M-H loop of CTCC powder

Fig. S20. M-H loop of the free-standing CTCC powder.

Dark and light-illuminated magnetism

Fig. S21. Magnetic and spin resonance properties of the cocrystal.

Magnetoelectric coupling

Fig. S22. Tunability of magnetization by electric field when the electric field is oriented perpendicular (A and C) and parallel (B and D) to the cocrystal long axis without (A and B) and with (C and D) light illumination.

References (*43*–*55*)

## REFERENCES AND NOTES


1. H. Miyasaka, Control of charge transfer in donor/acceptor metal–organic frameworks. *Acc. Chem. Res.* **46**, 248–257 (2013).
2. S. Ren, M. Wuttig, Organic exciton multiferroics. *Adv. Mater.* **24**, 724–727 (2012).
3. T. Enoki, A. Miyazaki, Magnetic TTF-based charge-transfer complexes. *Chem. Rev.* **104**, 5449–5478 (2004).
4. K. P. Goetz, A. Fonari, D. Vermeulen, P. Hu, H. Jiang, P. J. Diemer, J. W. Ward, M. E. Payne, C. S. Day, C. Kloc, V. Coropceanu, L. E. McNeil, O. D. Jurchescu, Freezing-in orientational disorder induces crossover from thermally-activated to temperature-independent transport in organic semiconductors. *Nat. Commun.* **5**, 5642 (2014).
5. K. P. Goetz, D. Vermeulen, M. E. Payne, C. Kloc, L. E. McNeil, O. D. Jurchescu, Charge-transfer complexes: New perspectives on an old class of compounds. *J. Mater. Chem. C* **2**, 3065–3076 (2014).
6. H. Liu, Q. Zhao, Y. Li, Y. Liu, F. Lu, J. Zhuang, S. Wang, L. Jiang, D. Zhu, D. Yu, L. Chi, Field emission properties of large-area nanowires of organic charge-transfer complexes. *J. Am. Chem. Soc.* **127**, 1120–1121 (2005).
7. S. K. Park, S. Varghese, J. H. Kim, S.-J. Yoon, O. K. Kwon, B.-K. An, J. Gierschner, S. Y. Park, Tailor-made highly luminescent and ambipolar transporting organic mixed stacked charge-transfer crystals: An isometric donor–acceptor approach. *J. Am. Chem. Soc.* **135**, 4757–4764 (2013).
8. T.-H. Lee, J.-H. Li, W.-S. Huang, B. Hu, J. C. A. Huang, T.-F. Guo, T.-C. Wen, Magnetoconductance responses in organic charge-transfer-complex molecules. *Appl. Phys. Lett.* **99**, 073307 (2011).
9. H. Alves, R. M. Pinto, E. S. Maçôas, Photoconductive response in organic charge transfer interfaces with high quantum efficiency. *Nat. Commun.* **4**, 1842 (2013).
10. L. Zhu, Y. Yi, Y. Li, E.-G. Kim, V. Coropceanu, J.-L. Brédas, Prediction of remarkable ambipolar charge-transport characteristics in organic mixed-stack charge-transfer crystals. *J. Am. Chem. Soc.* **134**, 2340–2347 (2012).
11. J. S. Miller, A. J. Arthur, W. M. William, Ferromagnetic molecular charge-transfer complexes. *Chem. Rev.* **88**, 201–220 (1988).
12. W. Qin, M. Gong, X. Chen, T. A. Shastry, R. Sakidja, G. Yuan, M. C. Hersam, M. Wuttig, S. Ren, Multiferroicity of carbon-based charge-transfer magnets. *Adv. Mater.* **27**, 734–739 (2015).
13. K. Kobayashi, S. Horiuchi, R. Kumai, F. Kagawa, Y. Murakami, Y. Tokura, Electronic ferroelectricity in a molecular crystal with large polarization directing antiparallel to ionic displacement. *Phys. Rev. Lett.* **108**, 237601 (2012).
14. G. Saito, T. Murata, Mixed valency in organic charge transfer complexes. *Philos. Trans. R. Soc. A* **366**, 139–150 (2008).
15. L. B. Coleman, M. J. Cohen, D. J. Sandman, F. G. Yamagishi, A. F. Garito, A. J. Heeger, Superconducting fluctuations and the Peierls instability in an organic solid. *Solid State Commun.* **12**, 1125–1132 (1973).
16. H. Alves, A. S. Molinari, H. X. Xie, A. F. Morpurgo, Metallic conduction at organic charge-transfer interfaces. *Nat. Mater.* **7**, 574–580 (2008).
17. J. M. Williams, A. J. Schultz, U. Geiser, K. D. Carlson, A. M. Kini, H. H. Wang, W.-K. Kwok, M.-H. Whangbo, J. E. Schirber, Organic superconductors—New benchmarks. *Science* **252**, 1501–1508 (1991).
18. I. G. Lezama, M. Nakano, N. A. Minder, Z. Chen, F. V. Di Girolamo, A. Facchetti, A. F. Morpurgo, Single-crystal organic charge-transfer interfaces probed using Schottky-gated heterostructures. *Nat. Mater.* **11**, 788–794 (2012).
19. A. S. Tayi, A. K. Shveyd, A. C. H. Sue, J. M. Szarko, B. S. Rolczynski, D. Cao, T. J. Kennedy, A. A. Sarjeant, C. L. Stern, W. F. Paxton, W. Wu, S. K. Dey, A. C. Fahrenbach, J. R. Guest, H. Mohseni, L. X. Chen, K. L. Wang, J. F. Stoddart, S. I. Stupp, Room-temperature ferroelectricity in supramolecular networks of charge-transfer complexes. *Nature* **488**, 485–489 (2012).
20. P. Lunkenheimer, J. Müller, S. Krohns, F. Schrettle, A. Loidl, B. Hartmann, R. Rommel, M. de Souza, C. Hotta, J. A. Schlueter, M. Lang, Multiferroicity in an organic charge-transfer salt that is suggestive of electric-dipole-driven magnetism. *Nat. Mater.* **11**, 755–758 (2012).
21. F. Kagawa, S. Horiuchi, M. Tokunaga, J. Fujioka, Y. Tokura, Ferroelectricity in a one-dimensional organic quantum magnet. *Nat. Phys.* **6**, 169–172 (2010).
22. W. Qin, X. Chen, H. Li, M. Gong, G. Yuan, J. C. Grossman, M. Wuttig, S. Ren, Room temperature multiferroicity of charge transfer crystals. *ACS Nano* **9**, 9373–9379 (2015).
23. R. Breslow, Stable 4n pi electron triplet molecules. *Pure Appl. Chem.* **54**, 927–938 (1982).
24. J. B. Torrance, S. Oostra, A. Nazzal., A new, simple model for organic ferromagnetism and the first organic ferromagnet. *Synthetic Met.* **19**, 709–714 (1987).
25. A. L. Briseno, S. C. B. Mannsfeld, S. A. Jenekhe, Z. Bao, Y. Xia, Introducing organic nanowire transistors. *Mater. Today* **11**, 38–47 (2008).
26. H. Li, B. C.-K. Tee, J. J. Cha, Y. Cui, J. W. Chung, S. Y. Lee, Z. Bao, High-mobility field-effect transistors from large-area solution-grown aligned $C_{60}$ single crystals. *J. Am. Chem. Soc.* **134**, 2760–2765 (2012).
27. D. H. Kim, J. T. Han, Y. D. Park, Y. Jang, J. H. Cho, M. Hwang, K. Cho, Single-crystal polythiophene microwires grown by self-assembly. *Adv. Mater.* **18**, 719–723 (2006).
28. M. Aryal, K. Trivedi, W. Hu, Nano-confinement induced chain alignment in ordered P3HT nanostructures defined by nanoimprint lithography. *ACS Nano* **3**, 3085–3090 (2009).
29. L. Wang, B. Liu, D. Liu, M. Yao, Y. Hou, S. Yu, T. Cui, D. Li, G. Zou, A. Iwasiewicz, B. Sundqvist, Synthesis of thin, rectangular $C_{60}$ nanorods using *m*-xylene as a shape controller. *Adv. Mater.* **18**, 1883–1888 (2006).
30. A. Das, S. Ghosh, Supramolecular assemblies by charge-transfer interactions between donor and acceptor chromophores. *Angew. Chem. Int. Ed.* **53**, 2038–2054 (2014).
31. W. Qin, D. Jasion, X. Chen, M. Wuttig, S. Ren, Charge-transfer magnetoelectrics of polymeric multiferroics. *ACS Nano* **8**, 3671–3677 (2014).
32. H. Sirringhaus, P. J. Brown, R. H. Friend, M. M. Nielsen, K. Bechgaard, B. M. W. Langeveld-Voss, A. J. H. Spiering, R. A. J. Janssen, E. W. Meijer, P. Herwig, D. M. de Leeuw, Two-dimensional charge transport in self-organized, high-mobility conjugated polymers. *Nature* **401**, 685–688 (1999).
33. Y. Kim, S. Cook, S. M. Tuladhar, S. A. Choulis, J. Nelson, J. R. Durrant, D. D. C. Bradley, M. Giles, I. McCulloch, C.-S. Ha, M. Ree, A strong regioregularity effect in self-organizing conjugated polymer films and high-efficiency polythiophene:fullerene solar cells. *Nat. Mater.* **5**, 197–203 (2006).
34. Y. Xie, Y. Li, L. Xiao, Q. Qiao, R. Dhakal, Z. Zhang, Q. Gong, D. Galipeau, X. Yan, Femtosecond time-resolved fluorescence study of P3HT/PCBM blend films. *J. Phys. Chem. C* **114**, 14590–14600 (2010).
35. L. Onsager, Initial recombination of ions. *Phys. Rev.* **54**, 554–557 (1938).
36. T. M. Clarke, J. R. Durrant, Charge photogeneration in organic solar cells. *Chem. Rev.* **110**, 6736–6767 (2010).
37. B. Hu, L. Yan, M. Shao, Magnetic-field effects in organic semiconducting materials and devices. *Adv. Mater.* **21**, 1500–1516 (2009).
38. W. Qin, M. Gong, T. Shastry, M. C. Hersam, S. Ren, Charge-transfer induced magnetic field effects of nano-carbon heterojunctions. *Sci. Rep.* **4**, 6126 (2014).
39. K. Vandewal, S. Albrecht, E. T. Hoke, K. R. Graham, J. Widmer, J. D. Douglas, M. Schubert, W. R. Mateker, J. T. Bloking, G. F. Burkhard, A. Sellinger, J. M. J. Fréchet, A. Amassian, M. K. Riede, M. D. McGehee, D. Neher, A. Salleo, Efficient charge generation by relaxed charge-transfer states at organic interfaces. *Nat. Mater.* **13**, 63–68 (2014).
40. L. He, M. Li, A. Urbas, B. Hu, Optically tunable magneto-capacitance phenomenon in organic semiconducting materials developed by electrical polarization of intermolecular charge-transfer states. *Adv. Mater.* **26**, 3956–3961 (2014).
41. J. N. Armstrong, S. Z. Hua, H. D. Chopra, Anisotropic Curie temperature materials. *Phys. Status Solidi B* **250**, 387–395 (2013).
42. J. van den Brink, D. I. Khomskii, Multiferroicity due to charge ordering. *J. Phys. Condens. Matter* **20**, 434217 (2008).
43. S. Plimpton, Fast parallel algorithms for short-range molecular dynamics. *J. Comput. Phys.* **117**, 1–19 (1995).
44. D. L. Cheung, D. P. McMahon, A. Troisi, Computational study of the structure and charge-transfer parameters in low-molecular-mass P3HT. *J. Phys. Chem. B* **113**, 9393–9401 (2009).
45. N. L. Allinger, Y. H. Yuh, J. H. Lii, Molecular mechanics. The MM3 force field for hydrocarbons. 1. *J. Am. Chem. Soc.* **111**, 8551–8566 (1989).
46. W. L. Jorgensen, D. S. Maxwell, J. Tirado-Rives, Development and testing of the OPLS all-atom force field on conformational energetics and properties of organic liquids. *J. Am. Chem. Soc.* **118**, 11225–11236 (1996).
47. V. Marcon, G. Raos, Molecular modeling of crystalline oligothiophenes: Testing and development of improved force fields. *J. Phys. Chem. B* **108**, 18053–18064 (2004).
48. L. A. Girifalco, Molecular properties of fullerene in the gas and solid phases. *J. Phys. Chem.* **96**, 858–861 (1992).
49. A. Cheng, M. L. Klein, C. Caccamo, Prediction of the phase diagram of rigid $C_{60}$ molecules. *Phys. Rev. Lett.* **71**, 1200–1203 (1993).
50. W. D. Cornell, P. Cieplak, C. I. Bayly, I. R. Gould, K. M. Merz, D. M. Ferguson, D. C. Spellmeyer, T. Fox, J. W. Caldwell, P. A. Kollman, A second generation force field for the simulation of proteins, nucleic acids, and organic molecules. *J. Am. Chem. Soc.* **117**, 5179–5197 (1995).
51. M. Bernardi, M. Giulianini, J. C. Grossman, Self-assembly and its impact on interfacial charge transfer in carbon nanotube/P3HT solar cells. *ACS Nano* **4**, 6599–6606 (2010).
52. W. Shinoda, M. Shiga, M. Mikami, Rapid estimation of elastic constants by molecular dynamics simulation under constant stress. *Phys. Rev. B* **69**, 134103 (2004).
53. J. M. Soler, E. Artacho, J. D. Gale, A. Garcia, J. Junquera, P. Ordejón, D. Sánchez-Portal, The SIESTA method for *ab initio* order-*N* materials simulation. *J. Phys. Condens. Matter* **14**, 2745–2779 (2002).
54. N. Troullier, J. L. Martins, Efficient pseudopotentials for plane-wave calculations. *Phys. Rev. B* **43**, 1993–2006 (1991).
55. J. Junquera, Ó. Paz, D. Sánchez-Portal, E. Artacho, Numerical atomic orbitals for linear-scaling calculations. *Phys. Rev. B* **64**, 235111 (2001).

**Acknowledgments:** We thank R. P. Dowd and T. Van Nguyen (Department of Chemical and Petroleum Engineering, University of Kansas) for their help on the c-AFM measurement. **Funding:** Work at the Temple University (S.R.) was supported by the Army Research Office Young Investigator Program (W911NF-15-1-0610, material design/self-assembly of carbon photovoltaics) and Department of Energy Basic Energy Sciences Award No. DE-FG02-13ER46937 (organic synthesis and physical property measurement). **Author contributions:** B.X. carried out experiments and wrote the paper. H.L. did the modeling calculation. A.H. measured the dielectric results, and M.G. took TEM images. W.G. and G.Y. did the PFM measurement. M.W., J.G., and S.R. guided the project and edited the paper. All authors discussed the results and commented on the manuscript. **Competing interests:** The authors declare that they have no competing interests. **Data and materials availability:** All data needed to evaluate the conclusions in the paper are present in the paper, and Supplementary Materials and will be made available by the authors upon request. Institutional Review Board and/or Institutional Animal Care and Use Committee guidelines were followed with human or animal subjects.

Submitted 11 September 2015
Accepted 30 October 2015
Published 18 December 2015
10.1126/sciadv.1501264

**Citation:** B. Xu, H. Li, A. Hall, W. Gao, M. Gong, G. Yuan, J. Grossman, S. Ren, All-polymeric control of nanoferronics. *Sci. Adv.* **1**, e1501264 (2015).

ScienceAdvances
AAAS

**All-polymeric control of nanoferronics**

Beibei Xu, Huashan Li, Asha Hall, Wenxiu Gao, Maogang Gong, Guoliang Yuan, Jeffrey Grossman and Shenqiang Ren (December 18, 2015)

*Sci Adv* 2015, 1:.
doi: 10.1126/sciadv.1501264